Prediction of different recrystallisation textures under a single unified physics-based model description

Traka, Konstantina; Hernández, Estefanía Sepúlveda; Nguyen-Minh, Tuan; Sedighiani, Karo; Sietsma, Jilt; Kestens, Leo A.I.

DOI
10.1016/j.commatsci.2024.113425

Publication date
2025

Document Version
Final published version

Published in
Computational Materials Science

Computational Materials Science 246 (2025) 113425

Contents lists available at ScienceDirect

Computational Materials Science

journal homepage: www.elsevier.com/locate/commatsci

Full length article

Prediction of different recrystallisation textures under a single unified physics-based model description

Konstantina Traka [a,*], Estefanía Sepúlveda Hernández [b,d], Tuan Nguyen-Minh [c], Karo Sedighiani [e], Jilt Sietsma [a], Leo A.I. Kestens [a,c]

[a] Department of Materials Science and Engineering, TU Delft, Mekelweg 2, 2628 CD Delft, The Netherlands
[b] Department of Electromechanical, Systems and Metal Engineering, Ghent University, Ghent, Belgium
[c] Metal Science and Technology, Department of Electromechanical, Systems and Metal Engineering, Ghent University, Technologiepark 46, B-9052 Ghent, Belgium
[d] Department of Metallurgical Engineering, Universidad de Santiago de Chile, Estacion Central, Chile
[e] Tata Steel, R&D, IJmuiden, The Netherlands

ARTICLE INFO

Dataset link: https://github.com/k-traka/OMicroN

Keywords:
Recrystallisation texture
Recrystallisation nucleation
Full-field simulation
Abnormal subgrain growth
Deformation temperature

ABSTRACT

This work investigates the formation of the recrystallisation microstructure and texture of various single-phase ferrite low-carbon steels that were rolled at different temperatures and of which the deformation microstructure was characterized by high resolution electron backscatter diffraction (EBSD). Three cases are considered: (i) cold-rolled interstitial-free (IF) steel, warm-rolled IF steel at 550 °C and warm rolled Fe-Si steel at 900 °C (below the austenitization temperature due to Si). It is well-known that the deformation texture after flat rolling of single-ferrite low carbon steels exhibits the characteristic α/γ-fiber texture, i.e. < 110 >//Rolling Direction (RD) and < 111 >//Normal Direction (ND), irrespective of the rolling temperature, as long as there is no concurrent phase transformation. However, different recrystallisation textures appear as a function of the rolling temperature. Generally speaking, the γ-fiber recrystallisation texture is obtained after cold rolling, whereas the θ-fiber components (< 100 >//ND) intensify at the expense of the γ-fiber orientations with increasing rolling temperature. Although these phenomena are well-known, the reasons for this behavior in terms of preferential orientation selection remain as yet unclear. In the present paper, recrystallisation microstructures and textures are simulated with a full-field cellular-automaton (CA) description, whereby recrystallisation from its incipient stage is considered as a process of sub-grain coarsening controlled by the well-known physical laws of driving force and kinetics. The simulations integrate in one single model the various conditions that give rise to the observed temperature dependence of the evolving static recrystallisation texture and microstructure. The different rolling temperatures will give rise to different initial microstructures at the onset of recrystallisation with noticeable variations in short-range orientation gradients in γ and θ-fiber orientations, respectively. The mere application of local grain-boundary migration laws on the topology of the deformation structure, without imposing any specific nucleation selection criterion, will properly balance the dominance of γ-fiber grains after cold-rolling and θ-fiber orientations after warm rolling. Finally, the well-known nucleation of Goss orientations ({110} < 001 >) in shear bands occurring in γ-fiber grains is also simulated in this single conceptual framework.

1. Introduction

As a phenomenon of high impact to the material properties (e.g. mechanical [1], or electro-magnetic [2]), but also as a strong tool to interpret the physical processes taking place, crystallographic texture formation is an integral part of our knowledge regarding recrystallisation (see for example reviews [3–14]). In ferritic low-carbon steels, recrystallisation typically enhances the so-called γ-fiber orientations, i.e. ⟨111⟩ // Normal Direction (ND) [15,16], whereas in some cases (e.g. at low strain rate or high rolling temperature), θ-fiber orientations (i.e. ⟨100⟩ // ND) appear or even dominate [9,17–21]. Owing to the orientation dependency of the stored deformation energy [22–27], these textures are commonly referred to as high stored-energy (γ-fiber) or low stored-energy (θ-fiber) recrystallisation textures.

From an industrial perspective, the occurrence of such different textures is beneficial, as it broadens the applicability, for example from

* Corresponding author.
E-mail address: C.Traka@tudelft.nl (K. Traka).

https://doi.org/10.1016/j.commatsci.2024.113425
Received 3 June 2024; Received in revised form 26 September 2024; Accepted 26 September 2024
Available online 7 October 2024

deep drawing (high stored-energy texture) to electromagnetic applications (low stored-energy texture). At the same time, the co-existence of these two different recrystallisation textures is very important because it reveals a contradiction, just as explained by Kestens and Pirgazi [13]: (a) γ-fiber orientations recrystallise because they constitute deformed grains of high orientation gradients and thus the subgrains have sufficient mobility and driving force to grow/nucleate and recrystallise [15], and (b) θ-fiber orientations recrystallise for the exact opposite reason, i.e. they are typically located at the least deformed grains, and can only grow or nucleate at the expense of the former.

While this contradiction has long been recognized, the physical processes leading to different recrystallisation behaviors remain unknown. Using interstitial free (IF) steel as example, in our own recent contribution [25] we showed that warm rolling leads to significant reductions in the short-range orientation gradients within γ-fiber grains, compared to cold rolling, while both the cold-rolled (CR) and the warm-rolled (WR) material exhibits the same trends in the distribution of stored energy. In the present work, we examine the impact of such different substructures on the subsequent recrystallisation behavior. Here, we use three different examples, i.e. (a) a cold-rolled (CR) interstitial free (IF) steel, (b) an IF steel warm-rolled at 550 °C (WR550), and (c) an Fe-Si steel warm-rolled at 900 °C (WR900). The addition of Si in the latter case is due to it acting as a ferrite stabilizer; it is not expected to have impact on the recrystallisation evolution in terms of texture formation.

The goal, here, is to address the reasons associated with the formation of low and high stored-energy recrystallisation textures, as well as identifying specific orientation components, by means of modeling, i.e. by investigating the simulated substructural and microstructural evolution. For this reason, we performed the simulations using a full-field model for (sub-)grain growth [28,29] in which no nucleation criterion is imposed. This means that a topological or kinetic advantage of certain subgrains does not only pertain to their initial status in comparison to the surrounding microstructure, as is the case when nucleation criteria are used [30–32], but it naturally occurs by the simulated evolving substructure, starting from the deformed state, as was for example done in [28,33]. The fact that we use a single and unified description for all recrystallisation-related phenomena (i.e. without adapting the model), which includes also the competitive subgrain growth leading to the so-called nucleation of subgrains, is what allows different types of annealing textures to be predicted.

The rise of different types of recrystallisation textures is then explained depending on the topological differences (misorientation, size) of the starting, and evolving, substructure. Specifically, using a one-to-one tracing and comparison of the continuously changing state variables, we obtain insight into the nucleation origin of well-known recrystallisation texture components.

2. Materials and methods

2.1. Materials and microstructures

2.1.1. Materials

The investigated materials are Ti-stabilized IF steel (cold-rolled and warm-rolled) and Fe-1.23 wt.%Si steel (warm-rolled). The addition of Si is not expected to have impact on the formation of the deformation substructure and the ensuing recrystallisation texture, but it allows for a relatively high rolling temperature without entailing the presence of austenite, as Si is a strong ferrite stabilizer.

Table 1 shows the material and processing parameters for the three different materials and Table 2 the characteristics of each scan obtained by electron backscatter diffraction (EBSD), serving as representative volume element (RVE) in this study.

Table 1
Materials used in the study.

Treatment code	Material	Rolling temperature	Thickness reduction
CR	IF steel	25 °C	80%
WR550	IF steel	550 °C	80%
WR900	Fe-Si	900 °C	80%

Table 2
Starting microstructures, obtained by EBSD, that are used in the simulations.

RVE name	Step/Mesh size δx	Scanned area RD × ND (per sample)
CR - sample 1	0.1 μm	50 μm × 50 μm
CR - sample 2	0.1 μm	50 μm × 50 μm
WR550 - sample 1	0.1 μm	100 μm × 50 μm
WR550 - sample 2	0.06 μm	50 μm × 100 μm
WR900	0.5 μm	1500 μm × 380 μm

2.1.2. Starting microstructures

The starting microstructures are obtained by EBSD and are imported in the modeling system (after filtering — namely by Grain CI standardization, Neighbor CI correlation, and Kuwahara [34,35] operations) in a one-to-one fashion, i.e. every model cell i assumes the crystal orientation of the EBSD pixel located at the same spatial coordinate. All microstructures and simulations are resolved in a hexagonal grid.

The starting microstructures are not decomposed into grains or subgrains prior to the simulation. Instead, the only state variable that plays a role in the simulation is the crystal orientation of each model cell i, and hence each model cell i is either a part of a subgrain or it is a subgrain in itself. Therefore, the plastic stored deformation energy accumulated in the material elements is not a state variable assigned in the interior of each model cell i, but it is reflected by the subgrain boundaries surrounding it.

Figs. 1 to 3 show the starting microstructures. The substructure at important areas for recrystallisation (e.g. grain boundaries, triple junctions, strong in-grain orientation gradients over short distances) is also shown — see selected areas in Figs. 1 to 3 on the left which are extracted and magnified (corresponding to the white boxes) from the RVE.

It is noteworthy that while the two CR samples (Fig. 1) are characterized by similar microstructural features (e.g. deformation bands, higher in-grain boundary density of some γ-fiber grains, etc.), the WR550 material exhibits differences between the two samples (see Fig. 2). For example, the first sample seems to have smaller orientation gradients in the γ-fiber grains (lower density of dark/black boundaries in the bluish grains of Fig. 2(a) compared to Fig. 2(b)), while the first sample has also regions that underwent dynamic or post-dynamic recrystallisation (see magnified area in Fig. 2(a)). This implies that there is deformation heterogeneity across the sheet, the origin of which is, however, not within the scope of this study. Therefore, each sample will be presented and discussed separately regarding the simulated recrystallisation evolution, considering its own prior deformed state.

As for the WR900 sample, from Fig. 3 it is clear that the in-grain color variations, and thus in-grain orientation gradients, are mild. Essentially, only deformed-grain boundaries appear as black (i.e. high misorientation).

2.1.3. Statistical relevance

Fig. 4 shows the $\phi_2 = 45°$ section of the orientation distribution function (ODF) for all materials used in this study. The left images (i.e. Fig. 4(a),(c),(e),(g),(i)) correspond to the whole RVE. Regarding the RVEs used, although the statistics are insufficient to discuss the macro-texture, the dominant deformation texture components, i.e. belonging to α- and γ-fiber, are present in all materials.

The right images (i.e. Fig. 4(b),(d),(f),(h),(j)) correspond to the pixels constituting the deformed grains of lower in-grain orientation

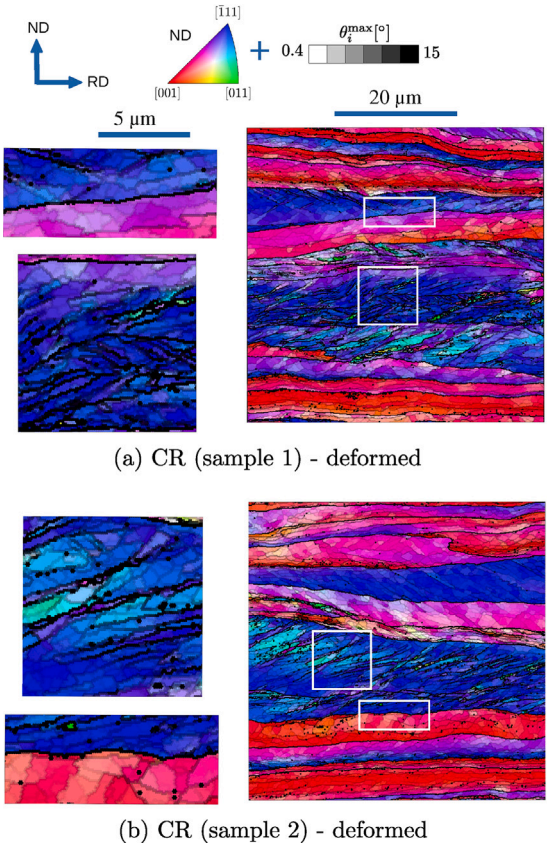

Fig. 1. Starting microstructure of the cold-rolled material shown for (a) sample 1 and (b) sample 2. The right images show the RVEs and the left images show the magnified regions (substructure) of the areas circumscribed on the right.

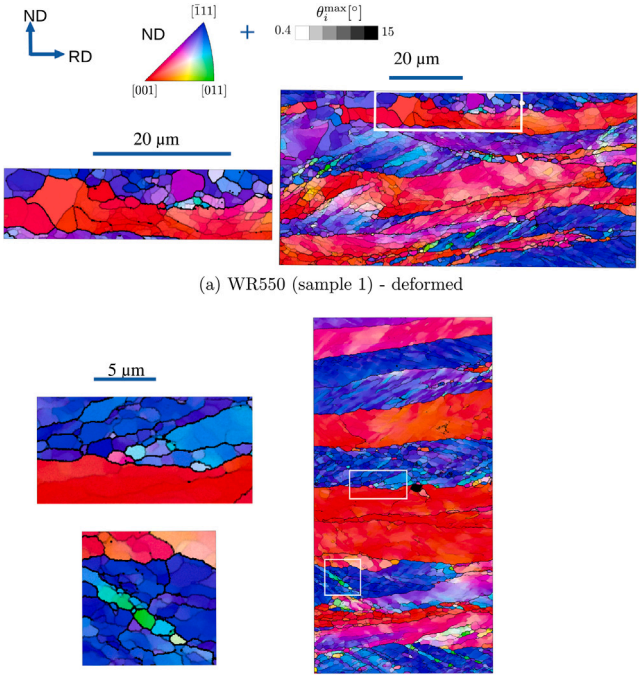

Fig. 2. Starting microstructure of the material warm-rolled at 550 °C (i.e. WR550) shown for: (a) sample 1 and (b) sample 2. The right images show the RVEs and the left images show the magnified regions (substructure) of the areas circumscribed on the right.

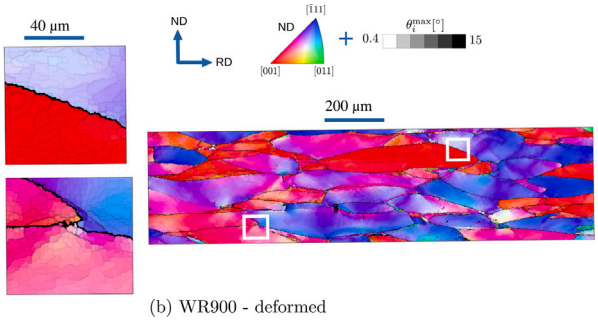

Fig. 3. Starting microstructure of the warm-rolled material at 900 °C (i.e. WR900). The right image shows the RVE and the left images show the magnified regions (substructure) of the areas circumscribed on the right.

scatter, quantified by the grain orientation spread (GOS[1] - the detailed quantification and the texture of the high GOS grains is shown in the supplementary material, also per sample). These ODFs are constructed from deformed grains with a GOS that is lower than the average GOS of the RVE. As is shown, the prior deformed grains characterized by lower stored energy, except for the WR550-sample 1, exhibit a soft Taylor texture, i.e. θ-fiber and (upper part) α-fiber. Therefore, the recrystallisation texture related to deformation trends are statistically captured. As for the WR550-sample shown in Fig. 4(e)(f), the low stored-energy ODF is very similar to the whole RVE's ODF, thus revealing a more homogeneous stored energy in terms of crystal orientation. However, even in this case, the low stored energy ODF comprises a slightly stronger rotated cube texture than the ODF of the whole RVE.

Also, it is noteworthy that the average GOS is 7.7–7.8°, 6.7–6.9°, 5.2°, in the CR, WR550, and WR900 samples, respectively, thus confirming the expected sequence of the stored-energy levels in the investigated materials.

Altogether, the statistics in relation to the orientation dependency of the stored deformation energy, as well as of the stored deformation energy levels inherent to the deformation processing parameters, are generally relevant to expected trends. Systematic analysis on the texture and plastic deformation of these materials can be found in [21, 25].

2.2. Model

2.2.1. Brief description

We use the model developed in [28,29], which is a full-field description of grain/subgrain growth, based on the deterministic cellular-automaton (CA) method [36,37]. The model is implemented in OMicroN (optimizing microstructures numerically), which is an open source program for full field microstructure simulations [28,38] and in CASIPT (cellular automata model for phase transformations) which is a full-field cellular automata model [28,38–41].

Essentially, it is a model applicable for grain growth and recrystallisation-related phenomena (nucleation, primary and secondary recrystallisation), as it is unbiased toward them. This means that all these phenomena occur naturally depending on the local substructure/microstructure without adapting the computational rules. An alternative mean field framework, though physically similar, can be found in [42,43].

[1] The GOS refers to the orientation spread considering all elements that belong to the same grain. Therefore, for the deformed state the decomposition of the microstructure in grains refers to large regions surrounded by high-angle grain boundaries (HAGBs), i.e. deformed grains, and it is used as a measure of the stored deformation energy of the main orientations constituting each grain.

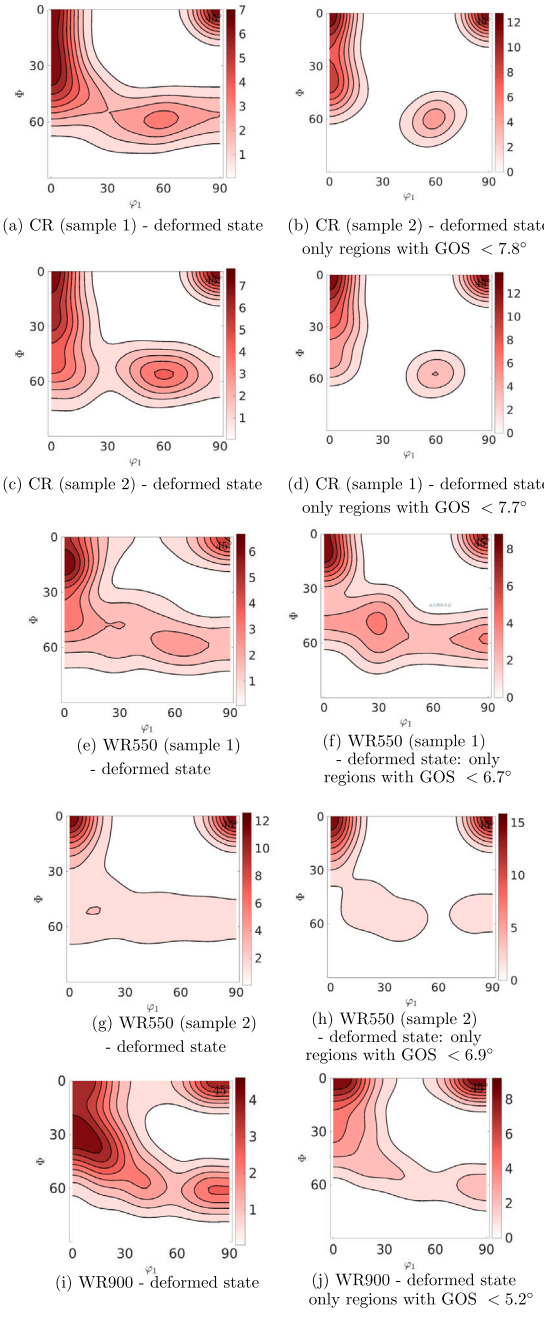

(a) CR (sample 1) - deformed state
(b) CR (sample 2) - deformed state only regions with GOS $< 7.8°$
(c) CR (sample 2) - deformed state
(d) CR (sample 1) - deformed state only regions with GOS $< 7.7°$
(e) WR550 (sample 1) - deformed state
(f) WR550 (sample 1) - deformed state: only regions with GOS $< 6.7°$
(g) WR550 (sample 2) - deformed state
(h) WR550 (sample 2) - deformed state: only regions with GOS $< 6.9°$
(i) WR900 - deformed state
(j) WR900 - deformed state only regions with GOS $< 5.2°$

Fig. 4. $\phi_2 = 45°$ section of the ODF of the deformed state for all samples (a, c, e, g, i) and for the subset of grains with GOS lower than the average in the RVE (b, d, f, h, j).

For example, if the microstructure comprises grains that are equiaxed, uniform, and without interior orientation gradients, the naturally simulated outcome is normal grain growth. Oppositely, in highly-resolved deformed microstructures, the accumulated plastic deformation is realized by in-grain orientation gradients and heterogeneities, i.e. subgrains misorientation and hence also size (since no misorientation between adjacent pixels means that they belong to the same subgrain). In this case, the competitive subgrain growth results in a simulated outcome that relates to recrystallisation phenomena. The recrystallised grains at any stage of the simulation are essentially the (sub)grains that were large and (more) mobile in comparison to their initial and changing neighborhood, i.e. they had an energy and kinetic advantage that led to their recrystallisation, just as explained in [28,44–48].

Any such pre-existing subgrain is in fact what we call "nucleus". Therefore, the model captures nucleation mechanisms inherent to the orientation gradients, i.e. stored energy related driving force and mobility, leading to: discontinuous subgrain growth and grain boundary bulging.

Regarding the computation time, this depends on the degree of accumulated plastic deformation of each sample, since the higher the orientation gradients, the more pixels are mobile and thereby are iterated for their possible re-orientation in each simulation step. In the present applications, the simulation time varies from 10 min to 2 h, in a 10-core computer with a 4.8 GHz Intel Core i7 processor with a 16 GB 3200 MHz memory. Since the model follows a deterministic framework, i.e. the results are repetitive, each application was computed once.

2.2.2. Computational rules

Regarding the modeling framework, the considered state variable of every element i is its crystal orientation g_i. Every pair of cells is considered to be separated by a boundary if the misorientation between them is larger than $\theta_{\min}$, which is equal to 0.4°, i.e. smaller misorientations are assumed to be noise. Specifically, a neighbor cell j can grow into cell i if the current energy of i (realized by the boundaries surrounding i), i.e. $E_i(g_i)$, is larger than the result if j grows into i, i.e. $E_i(g_j)$. In that case i transforms with a specific rate $\dot{f}_{g_i \to g_j}$ to its neighbor's orientation g_j.

The re-orientation rate of cell i to g_j comes from all k neighbors that can grow into i, i.e. with orientation g_k which is similar (with misorientation smaller than a threshold $\theta_{\min}$) to that of cell j. It is equal to:

$$\dot{f}_{g_i \to g_j} = \beta \cdot M_{g_i \to g_j} \cdot \sqrt{\sum_{r=x,y,z} \left(\sum_k \delta_{kj} \cdot \left| \Delta E_{g_i \to g_j} \cdot (A_{ik}/V_i) \cdot \vec{u}_{ik} \cdot \vec{u}_r \right| \right)^2} / V_i \quad (1)$$

and the associated energy release is:

$$\Delta E_{g_i \to g_j} = \sum_k A_{ik} \cdot (1 - \delta_{ik}) \cdot \gamma(g_i, g_k) - \sum_k (1 - c \cdot \delta_{lkij}) \cdot A_{ik} \cdot (1 - \delta_{jk}) \cdot \gamma(g_j, g_k) \quad (2)$$

where in Eqs. (1) and (2):

- k is an index meaning that cell k is neighbor of cell i.
- A_{ik} is the boundary area between elements i and k, and V_i the volume of i.
- $\gamma(g_i, g_k)$ is the energy density of the boundary between i and k, with value γ_{HAGB} for high angle grain boundaries (HAGB). For low angle grain boundaries (LAGBs) it depends on the misorientation based on Read and Shockley [49].
- δ_{ik} is a Kronecker-like operator taking the value 0 if the misorientation between i and k is more than the lower threshold $\theta_{\min}$, and 1 otherwise.
- c is a grid-related parameter (here equal to 0.7), that is activated based on a Kronecker-like operator δ_{lkij} which takes values of 1 if the misorientation between l and j is less than $\theta_{\min}$.
- $\vec{u}_r$ is the unit vector for the r axis of the reference system — here $r = \{x, y, z\}$ is such that for all samples x is the rolling direction (RD) and y is the normal direction (ND).
- $\vec{u}_{ki}$ is the unit vector normal to the boundary ik (in the CA grid).
- β is a grid-related constant (0.48 for this grid [29]), such that the CA kinetics match the theoretical thermally activated atomic jumps toward the planar boundary (short-range self-diffusion) explained by Turnbull [50], regardless of the mesh size and temperature.

Table 3
Input parameters.

Parameter	Value	Reference
γ_{HAGB}	0.5 J/m^2	[52]
$M_{0,\mathrm{HAGB}}$	0.8 mol m/(J s)	[28,29]
$Q_{g,\mathrm{HAGB}}$	140 kJ/mol	[53]
c	0.7	[28,29]
β	0.48	[29]

The mobility $M_{g_i \to g_j}$ for HAGBs is equal to:

$$M_{HAGB} = M_0 \cdot \exp\left(-Q_g / R \cdot T\right) \tag{3}$$

where M_0 is the pre-exponential factor and Q_g the activation energy for interface motion, R is the universal gas constant and T the temperature.

For LAGBs the mobility decreases with decreasing misorientation, based on [51]. More details on the derivation and meaning of each expression and term can be found in [29].

Table 3 shows the input parameters used in all applications in the present study.

Combining Eqs. (1) and (2) it becomes clear that:

- the heterogeneity in the growth rate comes from the misorientation throughout the substructure and microstructure. This is because it is related to the subgrains motion and hence preferential growth. In terms of the kinetic advantage the higher misorientation brings higher mobility, and in terms of energy/size advantage the energy density decreases for smaller misorientation up to the point that no misorientation means that pixels belong to the same subgrain (and thus size differences are also captured based on misorientation differences).
- the re-orientation rate increases quadratically with A_{ik}/V_i (Eqs. (1) and (2)), which means (a) that we have a constant area reduction rate, complying with the theory of curvature-driven grain coarsening explained by Mullins [54] and Von Neumann [55], and (b) that the kinetic outcome is not dependent on the grid spacing since $(A_{ik}/V_i)^2$ is inversely proportional to the square of the grid spacing.

2.2.3. Theoretical validation

Particularly for the aforementioned kinetic outcome and its relevance to the analytical theory, also for changing the mesh size, Fig. 5 shows the simulated outcome of an idealized RVE (i.e. a circular grain embedded in single larger grain) for four grid spacings δx and for the two different temperatures. The results are plotted together with the corresponding analytical theory by Smith [56] and Burke and Turnbull [57] for the same input parameters, i.e. the grain diameter evolution is $d = d_0 - 8 \cdot M \cdot \gamma$. As is shown, the modeled evolution matches well with the ideal circular shrinkage for both considered temperatures (and hence mobilities). Most importantly, the simulated data fit well with the theoretical expression of grain growth which confirms that indeed the grain's area reduces at a constant rate [54–64]. As for the grid spacing dependency, this is minor (considering the expected resolution dependency of grain growth in CA descriptions [64]), and only related to the resolution.

3. Results and discussion

3.1. Microstructure maps

Figs. 6 to 9 show the simulated temporal evolution of the microstructure for the different materials studied. The left images in Figs. 6 to 8 show the whole microstructure and the right images the simulated recrystallised regions, for the CR and WR550 samples, respectively. Similarly, for the WR900 sample, Fig. 9(a)(b)(c) show the whole microstructure and Fig. 9(d)(e) the recrystallised regions. The recrystallised grains are distinguished from the evolving substructure by separating the pixels belonging to very low GOS grains. Although there is no universal formula for such separation, as shown in Figs. 6 to 9 the distinction of recrystallised grains is rather straightforward, meaning that the recrystallised grains are the ones that do not have in-grain color variations (i.e. are without in-grain orientation gradients).

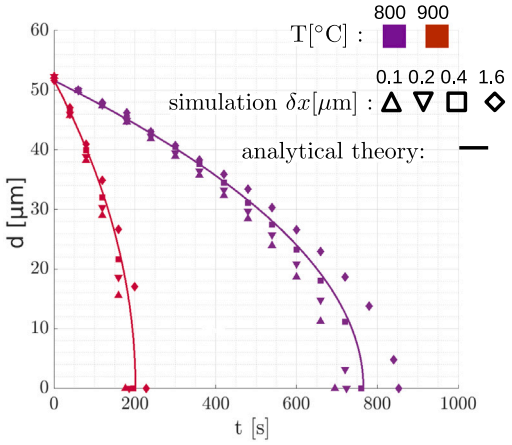

Fig. 5. Simulated outcome in comparison with analytical theory. The graph shows the simulated evolution of the shrinkage for a circular grain embedded in a single larger grain, at 800 °C and 900 °C, respectively.

Regarding the simulated recrystallisation evolution in the CR material, Fig. 6 shows that bluish grains (i.e. γ-fiber grains) dominate. For the cold-rolled material both samples exhibit similar simulated outcomes, which is why only one sample is shown here. Specifically, as the bluish grains are the fastest to recrystallise, the remaining unrecrystallised material (e.g. the regions that appear as white in the right images in Fig. 6) is mostly reddish (i.e. θ-fiber). This is a well known phenomenon regarding recrystallisation of CR low-carbon ferritic steels, which has been confirmed by many experimental observations, e.g. [27, 65].

For the WR550 samples, the simulated recrystallisation shown in Figs. 7 and 8 takes place differently. While the first WR550 sample (Fig. 7) recrystallises with mostly reddish grains (i.e. θ-fiber), the second WR550 sample (Fig. 8) is dominated by blueish recrystallised grains. This is in line with the deformed states, which as discussed earlier showed important differences between the two samples; especially only the second WR550 sample had strong orientation gradients within, at least some, of the deformed γ-fiber grains. This means that in-grain γ-fiber recrystallisation only takes place in the second WR550 sample.

Regarding the WR900 sample shown in Fig. 9, the largest recrystallised grains are reddish/pinkish, i.e. θ-fiber and/or close to α-fiber. It is noteworthy that while in the CR and WR550 samples each deformed grain becomes replaced by many distinct recrystallised grains, in the WR900 there are only a few recrystallised grains that can be distinguished whereas there are many prior deformed grains. For example, in Fig. 9(c) the size of the very few grains that can be easily distinguished as recrystallised is almost equal to the size of the prior deformed grains.

3.2. Texture change during recrystallisation

Fig. 10 shows the $\phi_2 = 45°$ section of the orientation distribution function (ODF) for all microstructures, from the deformed to the recrystallised stage.

The simulated recrystallised orientations seem to have very different characteristics, and particularly feature: (a) primarily orientations around the γ-fiber in the CR material, (b) primarily orientations around the θ-fiber in the WR550 – sample 1, whereas WR550 – sample 2 contains γ-fiber orientations, combined with strong rotated cube ($\{100\}\langle011\rangle$) and Goss ($\{110\}\langle001\rangle$) components, (c) primarily θ-fiber orientations in the WR900 material.

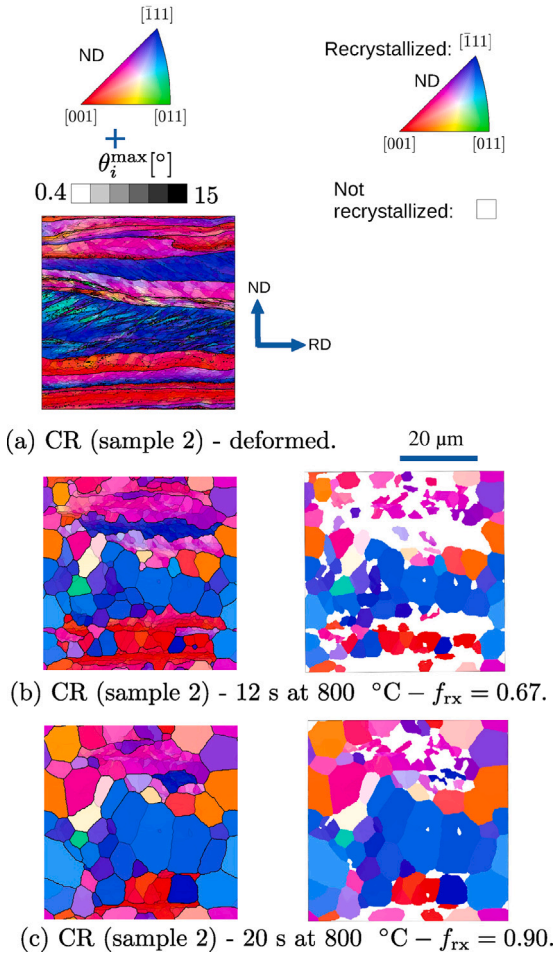

(a) CR (sample 2) - deformed.

(b) CR (sample 2) - 12 s at 800 °C – $f_{rx} = 0.67$.

(c) CR (sample 2) - 20 s at 800 °C – $f_{rx} = 0.90$.

Fig. 6. Simulated recrystallisation structure at 800°C in the CR material (sample 2).

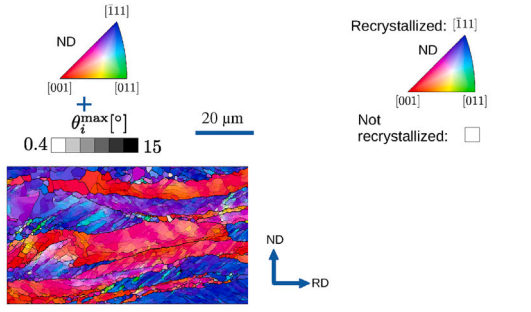

(a) WR550 (sample 1) - deformed.

(b) WR550 (sample 1) - 12 s at 800 °C – $f_{rx} = 0.28$.

(c) WR550 (sample 1) - 24 s at 800 °C – $f_{rx} = 0.70$.

Fig. 7. Simulated recrystallisation structure at 800° in the WR550 (sample 1).

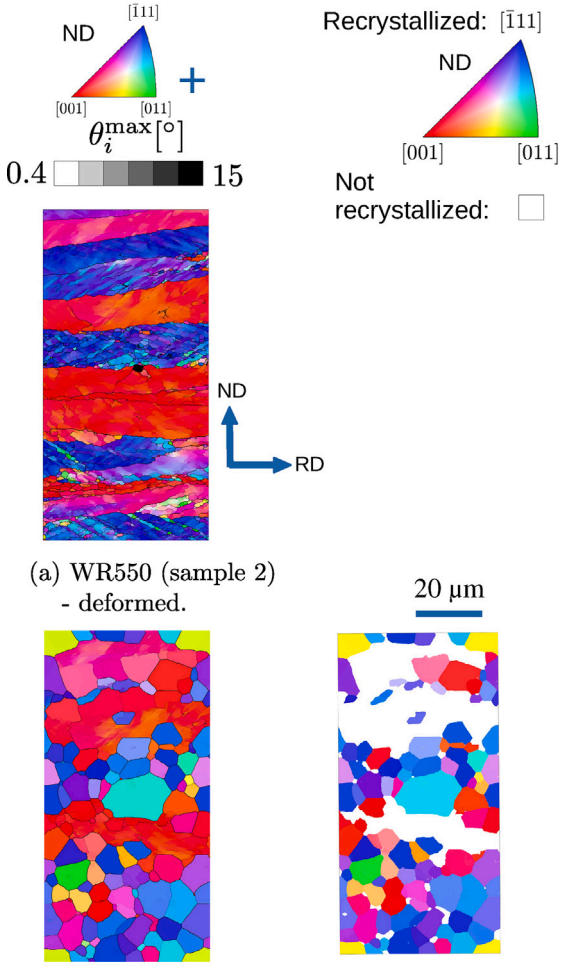

(a) WR550 (sample 2) - deformed.

(b) WR550 (sample 2) - 12 s at 800 °C – $f_{rx} = 0.70$.

(c) WR550 (sample 2) - 24 s at 800 °C – $f_{rx} = 0.88$.

Fig. 8. Simulated recrystallisation structure at 800° in the WR550 (sample 2).

The CR and the WR900 simulated recrystallisation textures constitute clear trends of high and low stored-energy texture developments. As for the WR550 material, the macro-texture formation is unclear, due to (a) the already strong(er) cube texture in the deformed state, in comparison to the other two materials, and (b) the large statistical scatter, caused by the differences in the deformed state of the two samples.

Despite the scatter and the limited statistics that do not allow for a discussion at the level of the full sheet texture, the simulated results do agree with the experimentally observed texture formation trends [9,

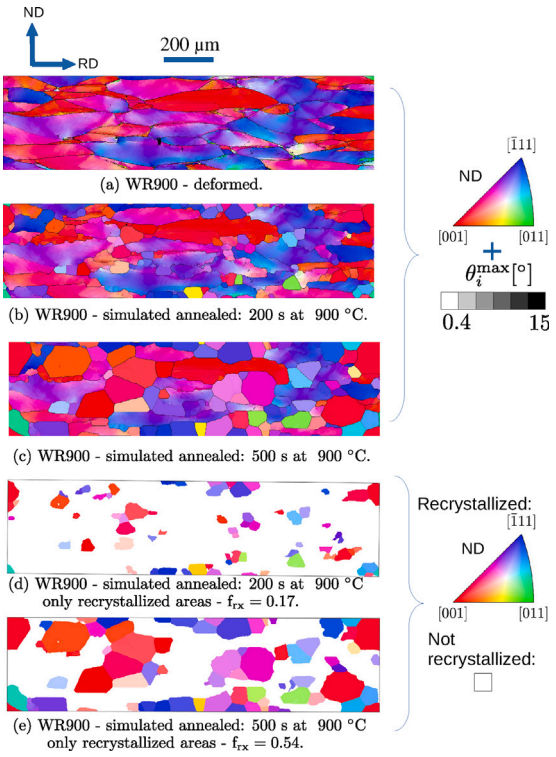

Fig. 9. Simulated recrystallisation structure at 900° in the WR900 material.

13,15–21]. Specifically, it is expected that from the cold-rolled recrystallisation texture characterized by γ-fiber texture, increasing the deformation temperature leads to a weakening of the γ-fiber texture. This trend was confirmed by the simulations, since only the CR material is dominated exclusively by γ-fiber components in the recrystallised state, while the WR550 material is characterized by mixed γ-fiber and θ-fiber, and the WR900 by mostly θ-fiber orientations.

3.3. Competitive subgrain growth and associated nucleation mechanisms

This section investigates the evolution and mesoscale competition of the dominant simulated nucleation mechanisms, i.e. the competition between in-grain nucleation (discontinuous subgrain growth and shear band nucleation) and grain boundary bulging.

Figs. 11, 12, and 13 show the simulated recrystallisation at the early stages for the CR, WR550, and WR900 material, respectively. Re-oriented pixels are plotted with crystal direction parallel to ND (i.e. IPF//ND) while cells that have not changed their initial orientation by more than 10° are plotted as white.

In the cold-rolled material (Fig. 11) both grain boundary bulging and discontinuous subgrain growth occur. Re-oriented pixels appearing along the prior deformed grain boundaries are indicative of the bulging of subgrains (see e.g. black arrows in Fig. 11). Fig. 11(b)(e) show the orientations after annealing for the cells which have been re-oriented. Fig. 11(c)(f) show the initial orientation of the cells which have been re-oriented. It is clear that here grain boundary bulging mostly favors the θ-fiber recrystallisation, i.e. prior bluish elements (γ-fiber) along the grain boundary are replaced by reddish colored grains (θ-fiber).

At the same time, the in-grain recrystallisation in the cold-rolled material is much more pronounced, e.g. see the circumscribed γ-fiber grains in Fig. 11. Here, the initially blueish elements recrystallise into other blueish elements, thus revealing the discontinuous subgrain growth taking place between γ-fiber components of high misorientation. Eventually, it is obvious that the simultaneous discontinuous subgrain growth (i.e. in-grain recrystallisation of primarily γ-fiber grains)

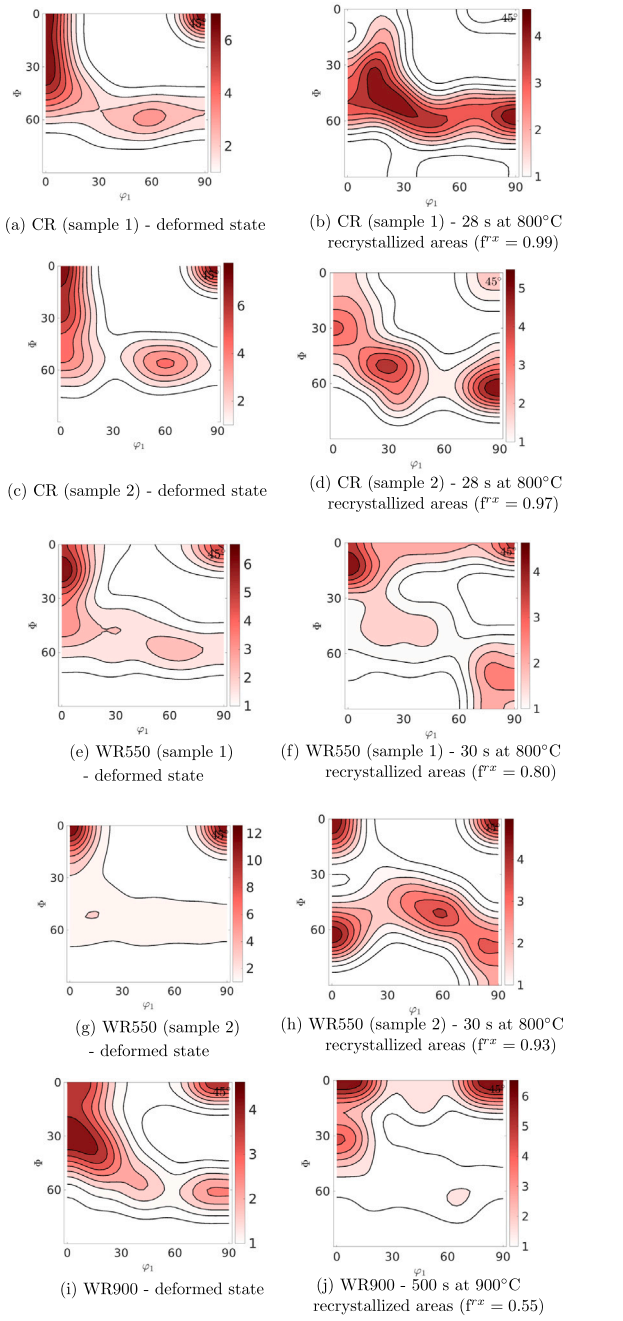

Fig. 10. Section $\phi_2 = 45°$ of the ODF quantified for all materials. The left images correspond to the deformed state and the right images to the recrystallised state. For the latter cases the ODFs are quantified only for the simulated recrystallised areas.

prevails over the above-mentioned grain boundary bulging. As already shown in [28], this explains the associated γ-fiber recrystallisation texture formation.

In the WR550 material (Fig. 12) the nucleation stage takes place somewhat differently between the two samples. The second sample shows a combined grain boundary bulging of θ-fiber (see in Fig. 12(d)–(f) the black arrows pointing at the reddish elements that consume the initially blueish ones) and discontinuous subgrain growth (see the blueish grains circumscribed in Fig. 12(d)–(f)). In contrast, in the first sample discontinuous subgrain growth is almost entirely absent, and it is clear that most subgrains recrystallise by bulging, and primarily belong to the θ-fiber. This also explains the difference observed earlier in the simulated textures (i.e. Fig. 10(f) versus Fig. 10(h)).

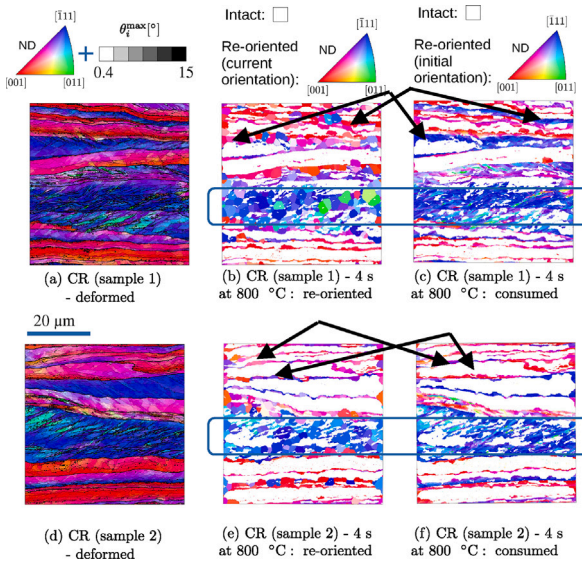

Fig. 11. Simulated nucleation in the cold-rolled material. The cells that have changed their initial orientation by more than 10° are color-coded with IPF//ND whereas the cells with orientation close to (i.e. less than 10° from) their initial orientation are plotted as white.

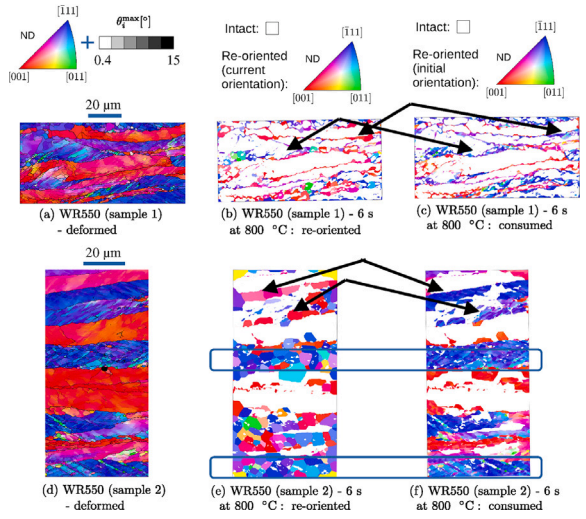

Fig. 12. Simulated nucleation in the WR550 material. The cells that have been surpassed at least once by a boundary more than 10° are color-coded with IPF//ND whereas the cells with orientation close to (i.e. less than 10° from) their initial orientation are plotted as white.

In the WR900 material (Fig. 13) the only nucleation mechanism taking place is grain boundary bulging. This is due to the absence of strong in-grain orientation gradients, which makes only deformed-grain boundaries mobile. Here, the subgrains bulge through almost all available grain boundaries, i.e. red-to-purple, purple-to-red, purple-to-blue, blue-to-purple, as pointed out by the black arrows in Fig. 13. Consequently, it is expected that the recrystallisation texture formation in the WR900 material takes place at the incipient stages.

3.4. Subgrains/nuclei responsible for the dominant fiber formation

This section reviews the origin of recrystallised grains in the CR and WR900 materials, used as two extreme examples of low and high stored-energy texture. Figs. 14 and 15 show the surrounding substructure and exact location of prior subgrains that become recrystallised grains.

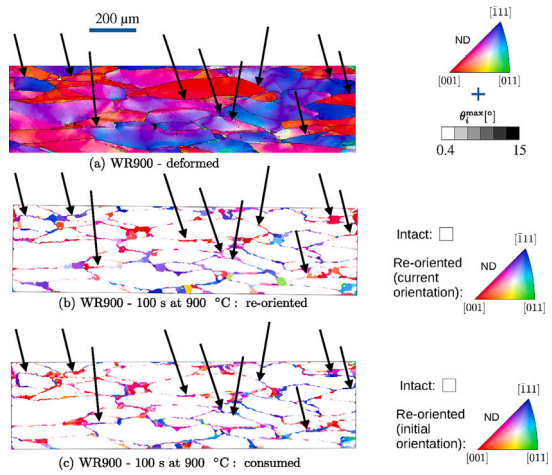

Fig. 13. Simulated nucleation in the WR900 material. The cells that have been surpassed at least once by a boundary more than 10° are color-coded with IPF//ND whereas the cells with orientation close to (i.e. less than 10° from) their initial orientation are plotted as white.

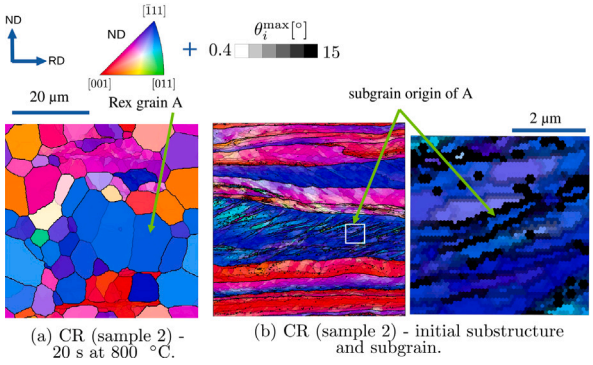

Fig. 14. Simulated recrystallisation in the CR material and its origin (i.e. prior subgrain), (a) shows a recrystallised grain selected, and (b) shows its origin: the left image shows the location within the RVE and the right the magnified region of the relevant substructure. The arrow in the points at the exact subgrain that becomes the recrystallised grain A.

3.4.1. Discontinuous subgrain growth - γ-fiber

In Fig. 14, a typical example of γ-fiber recrystallisation texture is shown where a grain, indicated as grain A, recrystallises via discontinuous subgrain growth. The crystal orientation is close to the nominal $\{111\}\langle 112\rangle$ component. As is shown, this grain originates from a subgrain surrounded by high-angle boundaries (at least partially) and small subgrains. These two give a kinetic and energy advantage to the subgrains that grow "competitively" and thus nucleate and recrystallise.

3.4.2. Grain boundary/triple junction nucleation - θ-fiber

Fig. 15 shows the origin of four recrystallised grains — all among the largest. The crystal orientations are (close to the nominal): rotated cube, i.e. $\{001\}\langle 110\rangle$ (grains A and D), $\{113\}\langle 110\rangle$ (grain B), and cube $\{001\}\langle 100\rangle$ (grain C). Out of these four, only grain D nucleates via bulging of a relatively flat boundary. In fact, grains A, B, and C nucleate via the bulging of the A,B, C subgrains at triple junctions.

3.5. Subgrains/nuclei responsible for specific orientation components

3.5.1. Goss orientation - $\{110\}\langle 001\rangle$

In Fig. 16, the subgrain origin of three recrystallised grains in the WR550 material is shown - Fig. 16(a) corresponds to the first sample and Fig. 16(b) to the second. Here, we choose only grains close to the

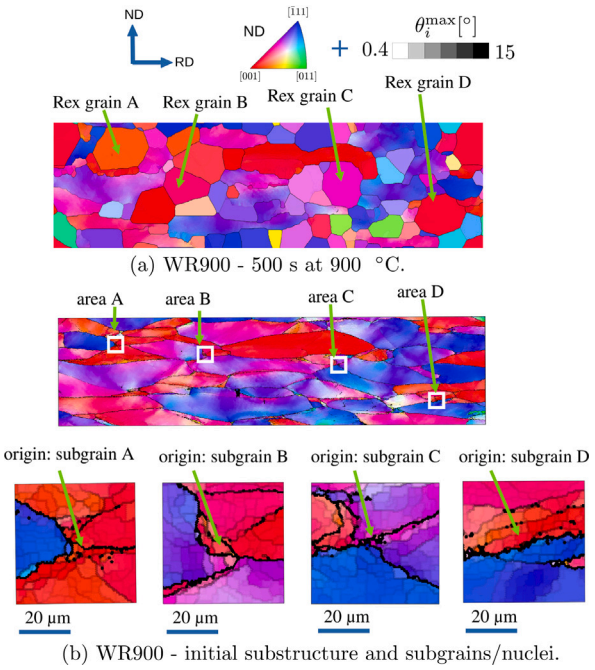

Fig. 15. Simulated recrystallisation in the WR900 material and its origin (prior subgrain), (a) shows the recrystallised grains selected, and (b) shows their origin: the top row shows the location within the RVE and the bottom row the magnified regions of the relevant substructure. The arrows in the bottom row show the exact subgrains that become recrystallised grains (A, B, C, D)

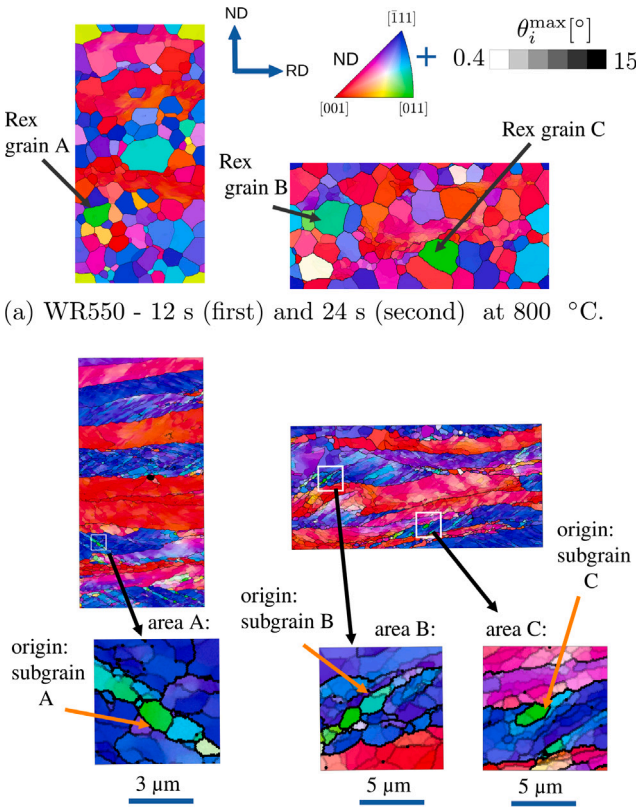

Fig. 16. Simulated recrystallisation in the WR550 material and its origin (prior subgrains), (a) shows the recrystallised grains selected, and (b) shows their origin: the top row shows the location within the RVEs and the bottom row the magnified regions of the relevant substructure. The arrows in the bottom row show the exact subgrains that become recrystallised grains (A, B, C).

nominal Goss component, i.e. {110}⟨001⟩, since its nucleation, and the mechanism leading to it, was confirmed in both samples. Specifically, it is clear from Fig. 16 that Goss-oriented subgrains recrystallise from shear bands within the γ-fiber grains, and it is shown that these subgrains are surrounded by HAGBs at the rims of the shear band where they meet γ-fiber components, as well as within the shear bands where strong orientation gradients have developed. Although the shear band nucleation of Goss orientations has already been explained much earlier by Ushioda and Hutchinson [66], the simulated outcome confirms also the theoretical basis of Goss recrystallisation in view of its kinetic advantage, and later size advantage due to its continuous rapid expansion, when constituting shear bands.

In contrast to the CR material, in this warm-rolled material, the γ-fiber discontinuous subgrain growth competes also with shear band nucleation (Goss orientations), which forms an additional reason for the γ-fiber weakening of the annealing texture.

3.5.2. *Crystal orientations* {311}⟨136⟩ – {411}⟨148⟩

Regarding the recrystallisation of {311}⟨136⟩ – {411}⟨148⟩ grains, the statistics are not optimal, i.e. the simulated recrystallised state comprises only a few grains for each RVE, out of which only one or two belong to the {311}⟨136⟩ – {411}⟨148⟩ component. Nevertheless, for these four recrystallised {311}⟨136⟩ – {411}⟨148⟩ grains (see pink-colored grains in Fig. 17) it becomes clear that none of these grains originates from a conventional nucleation mechanism.

In the two samples of the WR550 material (grains B, C, D in Fig. 17) the prior subgrains that nucleate are all located in the substructure separating the γ-fiber and the θ-fiber orientations. In all these cases the substructure is characterized by a high orientation spread, where the {311}⟨136⟩ – {411}⟨148⟩ subgrains are surrounded by HAGBs and have a distinct size advantage.

In the CR material (Fig. 17(a) and (d)), the {311}⟨136⟩ – {411}⟨148⟩ subgrain that recrystallises is located within the α-fiber grain. The substructure surrounding it, nonetheless, exhibits high orientation spread. Within a few micrometers distance the pink growing subgrain encounters highly misoriented subgrains of α-fiber and Goss. Additionally, the exact location of the subgrain is next to a shear band (indicated by blue arrow in Fig. 17(b)) within the α-fiber grain.

It can be concluded that all four {311}⟨136⟩ – {411}⟨148⟩ grains that recrystallise originate from highly fragmented regions, in the grain interior or close to the grain boundary of otherwise soft Taylor grains. Following up on the debate between stored-energy driven and selective growth explained in [13], the {311}⟨136⟩ recrystallisation can be explained by its fast growth inside {211}⟨110⟩ [67] due to the 26.5°⟨110⟩ Ibe and Lücke [68] orientation relationship. Nevertheless, since here the latter phenomenon is not considered, substantiating the observations of Gobernado et al. [69], the {311}⟨136⟩ – {411}⟨148⟩ recrystallisation is associated with the highly deformed substructure of otherwise low stored-energy grains.

4. Conclusions

In this work, we investigated the recrystallisation evolution in ferritic low carbon steel, by simulating and tracing the competitive subgrain growth taking place. Nucleation is not imposed in the simulation (i.e. the simulations are done using a (sub)grain growth model) and hence the recrystallised grains originate from subgrains that have a kinetic and energy advantage. We emphasized the texture evolution (dominant fibers and specific components) in relation to the nucleation mechanism.

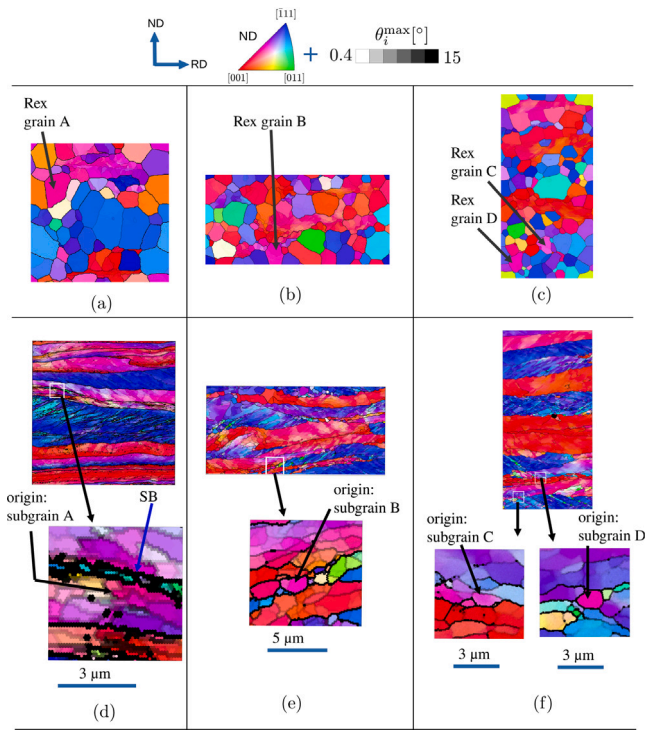

Fig. 17. Simulated partially recrystallised state in all materials, showing the recrystallisation of $\{311\}\langle 136\rangle - \{411\}\langle 148\rangle$ grains; (a),(b),(c) show the selected recrystallised grains for the CR, WR550 -sample 1, and WR550-sample 2, and (d),(e),(f) show their origin for the CR, WR550 -sample 1, and WR550-sample 2. In (d),(e),(f) the top row shows the location within the RVEs and the bottom row the magnified regions of the relevant substructure. The arrows in the bottom row show the exact subgrains that become recrystallised grains (A, B, C, D).

We used differently deformed materials (starting from cold rolled up to deformation at very high temperature) in order to compare the recrystallisation texture in close coupling with the different deformation features inherent to the rolling. The main findings are:

- The model can simulate the recrystallisation evolution in the various deformed materials of very different substructures, and results in very different texture-formation trends, in accordance with the experimental evidence.
- Our model simulates and captures well-known texture phenomena, including the recrystallisation of high stored-energy components (i.e. γ-fiber), low stored-energy components (i.e. θ-fiber), the Goss orientation, and the $\{311\}\langle 136\rangle - \{411\}\langle 148\rangle$ component. Hence, all these texture formation phenomena can be explained under a single physics-based description.
- In the cold-rolled material recrystallisation takes place via discontinuous subgrain growth and grain boundary bulging. The discontinuous subgrain growth is dominant over the other mechanisms, and thus gives rise to a distinct γ-fiber texture.
- In the material rolled at 550 °C recrystallisation takes place via discontinuous subgrain growth, grain boundary bulging, and shear band nucleation. Here, the competition is more in balance, thus giving rise to γ-fiber (discontinuous subgrain growth), rotated cube (grain boundary bulging), and Goss orientations (shear band nucleation).
- In the material rolled at 900 °C recrystallisation takes place only via grain boundary bulging, particularly at triple junctions. The associated crystal orientations belong to the θ-fiber and soft α-fiber components.

CRediT authorship contribution statement

Konstantina Traka: Writing – original draft, Validation, Software, Methodology, Investigation, Formal analysis, Conceptualization. **Estefanía Sepúlveda Hernández:** Writing – review & editing, Investigation, Data curation, Conceptualization. **Tuan Nguyen-Minh:** Writing – review & editing, Investigation, Conceptualization. **Karo Sedighiani:** Writing – review & editing, Investigation. **Jilt Sietsma:** Writing – review & editing, Supervision, Resources, Investigation, Formal analysis, Conceptualization. **Leo A.I. Kestens:** Writing – review & editing, Supervision, Resources, Project administration, Investigation, Funding acquisition, Formal analysis, Conceptualization.

Declaration of competing interest

The authors declare that they have no known competing financial interests or personal relationships that could have appeared to influence the work reported in this paper.

Data availability

The code used in the present study (OMicroN) can be found in: https://github.com/k-traka/OMicroN.

Acknowledgments

The authors greatfully acknowledge the support of the National Agency for Research and Development (ANID-Chile)/Doctorado Nacional/2021– 21210158. The authors are very greatful to Professor Dierk Raabe (MPIE Düsseldorf) for the constructive discussions and feedback.

Appendix A. Supplementary data

Supplementary material related to this article can be found online at https://doi.org/10.1016/j.commatsci.2024.113425.

References

[1] T.W. Lankford, S. Snyder, J.A. Bausher, New criteria for predicting the press performance of deep drawing sheets, Trans. Am. Soc. Met. 42 (1950) 1197–1205.
[2] A.D. Rollett, M.L. Storch, E.J. Hilinski, S.R. Goodman, Approach to saturation in textured soft magnetic materials, Metall. Mater. Trans. A 32 (10) (2001) 2595–2603, http://dx.doi.org/10.1007/s11661-001-0049-2, ISSN 1073-5623, 1543-1940. URL https://link.springer.com/10.1007/s11661-001-0049-2.
[3] W.B. Hutchinson, Development and control of annealing textures in low-carbon steels, Int. Met. Rev. 29 (1) (1984) 25–42, http://dx.doi.org/10.1179/imtr.1984.29.1.25, ISSN 0308-4590. URL http://www.tandfonline.com/doi/full/10.1179/imtr.1984.29.1.25.
[4] M. Hölscher, D. Raabe, K. Lücke, Rolling and recrystallization textures of bcc steels, Steel Res. Int. 62 (12) (1991) 567–575.
[5] D. Raabe, K. Lücke, Annealing textures of BCC metals, Scr. Metall. Mater. 27 (11) (1992) 1533–1538, http://dx.doi.org/10.1016/0956-716X(92)90140-A, ISSN 0956716X. URL https://linkinghub.elsevier.com/retrieve/pii/0956716X9290140A.
[6] R.K. Ray, J.J. Jonas, R.E. Hook, Cold rolling and annealing textures in low carbon and extra low carbon steels, Int. Mater. Rev. 39 (4) (1994) 129–172, http://dx.doi.org/10.1179/imr.1994.39.4.129, ISSN 0950-6608, 1743-2804. URL http://www.tandfonline.com/doi/full/10.1179/imr.1994.39.4.129.
[7] R.D. Doherty, D.A. Hughes, F.J. Humphreys, J.J. Jonas, D. Jensen, M.E. Kassner, W.E. King, T.R. McNelley, H.J. McQueen, A.D. Rollett, Current issues in recrystallization: a review, Mater. Sci. Eng. A 238 (2) (1997) 219–274, http://dx.doi.org/10.1016/S0921-5093(97)00424-3, ISSN 09215093. URL https://linkinghub.elsevier.com/retrieve/pii/S0921509397004243.
[8] B. Hutchinson, D. Artymowicz, Advances in physical metallurgy and processing of steels. mechanisms and modelling of microstructure/texture evolution in interstitial-free steel sheets, ISIJ Int. 41 (6) (2001) 533–541, http://dx.doi.org/10.2355/isijinternational.41.533, ISSN 0915-1559. URL http://joi.jlc.jst.go.jp/JST.Journalarchive/isijinternational1989/41.533?from=CrossRef.
[9] D. Stojakovic, R.D. Doherty, S.R. Kalidindi, F.J.G. Landgraf, Thermomechanical processing for recovery of desired {001} fiber texture in electric motor steels, Metall. Mater. Trans. A 39 (7) (2008) 1738–1746, http://dx.doi.org/10.1007/s11661-008-9525-2, ISSN 1073-5623, 1543-1940. URL https://link.springer.com/10.1007/s11661-008-9525-2.

[10] A. Haldar, S. Suwas, D. Bhattacharjee (Eds.), Microstructure and Texture in Steels, Springer London, London, 2009, http://dx.doi.org/10.1007/978-1-84882-454-6, ISBN 978-1-84882-453-9 978-1-84882-454-6. URL http://link.springer.com/10.1007/978-1-84882-454-6.

[11] B.J. Duggan, Y.Y. Tse, G. Lam, M.Z. Quadir, Deformation and recrystallization of interstitial free (IF) steel, Mater. Manuf. Process. 26 (1) (2011) 51–57, http://dx.doi.org/10.1080/10426910903202237, ISSN 1042-6914, 1532-2475. URL http://www.tandfonline.com/doi/abs/10.1080/10426910903202237.

[12] D. Raabe, Recovery and recrystallization: Phenomena, physics, models, simulation, in: Physical Metallurgy, Elsevier, 2014, pp. 2291–2397, ISBN 978-0-444-53770-6. URL https://linkinghub.elsevier.com/retrieve/pii/B978044453770600023X.

[13] L.A.I. Kestens, H. Pirgazi, Texture formation in metal alloys with cubic crystal structures, Mater. Sci. Technol. 32 (13) (2016) 1303–1315, http://dx.doi.org/10.1080/02670836.2016.1231746, ISSN 0267-0836, 1743-2847. URL https://www.tandfonline.com/doi/full/10.1080/02670836.2016.1231746.

[14] K. Ushioda, Advances in research on deformation and recrystallization for the development of high-functional steels, Sci. Technol. Adv. Mater. 21 (1) (2020) 29–42, http://dx.doi.org/10.1080/14686996.2019.1710013, ISSN 1468-6996, 1878-5514. URL https://www.tandfonline.com/doi/full/10.1080/14686996.2019.1710013.

[15] I.L. Dillamore, C.J.E. Smith, T.W. Watson, Oriented nucleation in the formation of annealing textures in iron, Met. Sci. J. 1 (1) (1967) 49–54, http://dx.doi.org/10.1179/msc.1967.1.1.49, ISSN 0026-0681. URL https://www.tandfonline.com/doi/full/10.1179/msc.1967.1.1.49.

[16] I. Samajdar, B. Verlinden, P. Van Houtte, D. Vanderschueren, γ-Fibre recrystallization texture in IF-steel: an investigation on the recrystallization mechanisms, Mater. Sci. Eng. A 238 (2) (1997) 343–350, http://dx.doi.org/10.1016/S0921-5093(97)00455-3, ISSN 09215093. URL https://linkinghub.elsevier.com/retrieve/pii/S0921509397004553.

[17] Y. Inokuti, R.D. Doherty, Transmission kossel study of the structure of cold-rolled iron and its nucleation behaviour, Texture Cryst. Solids 2 (3) (1977) 143–168, http://dx.doi.org/10.1155/TSM.2.143, ISSN 0309-7951. URL http://www.hindawi.com/archive/1977/356284/abs/.

[18] L. Kestens, J.J. Jonas, P. Van Houtte, E. Aernoudt, Orientation selective recrystallization of nonoriented electrical steels, Metall. Mater. Trans. A 27 (8) (1996) 2347–2358, http://dx.doi.org/10.1007/BF02651889, ISSN 1073-5623, 1543-1940. URL https://link.springer.com/10.1007/BF02651889.

[19] M.R. Barnett, J.J. Jonas, Influence of ferrite rolling temperature on microstructure and texture in deformed low C and IF steels, ISIJ Int. 37 (7) (1997) 697–705, http://dx.doi.org/10.2355/isijinternational.37.697, ISSN 0915-1559. URL http://www.jstage.jst.go.jp/article/isijinternational1989/37/7/37_7_697/_article.

[20] K. Murakami, J. Tarasiuk, H. Regle, B. Bacroix, Study of the texture formation during strain induced boundary migration in electrical steel sheets, in: Materials Science Forum, vol. 467, Trans Tech Publ, 2004, pp. 893–898.

[21] T. Nguyen Minh, J.J. Sidor, R.H. Petrov, L. Kestens, Texture evolution during asymmetrical warm rolling and subsequent annealing of electrical steel, Mater. Sci. Forum 702–703 (2011) 758–761, http://dx.doi.org/10.4028/www.scientific.net/MSF.702-703.758, ISSN 1662-9752. URL https://www.scientific.net/MSF.702-703.758.

[22] L. Kestens, J.J. Jonas, Modeling texture change during the static recrystallization of interstitial free steels, Metall. Mater. Trans. A 27 (1) (1996) 155–164, http://dx.doi.org/10.1007/BF02647756, ISSN 1073-5623, 1543-1940. URL http://link.springer.com/10.1007/BF02647756.

[23] K. Sedighiani, V. Shah, K. Traka, M. Diehl, F. Roters, J. Sietsma, D. Raabe, Large-deformation crystal plasticity simulation of microstructure and microtexture evolution through adaptive remeshing, Int. J. Plast. 146 (2021) 103078, http://dx.doi.org/10.1016/j.ijplas.2021.103078, ISSN 07496419. URL https://linkinghub.elsevier.com/retrieve/pii/S0749641921001509.

[24] K. Sedighiani, Crystal Plasticity Simulation of Microstructure and Microtexture Evolution during Large Plastic Deformation (Ph.D. thesis), Delft University of Technology, Netherlands, 2022.

[25] E. Sepúlveda Hernández, T. Nguyen-Minh, K. Traka, F. Castro Cerda, L.A.I. Kestens, Orientation dependence of dynamic compared to static recovery in interstitial free steel, Scr. Mater. 249 (2024) 116151, http://dx.doi.org/10.1016/j.scriptamat.2024.116151, ISSN 13596462. URL https://linkinghub.elsevier.com/retrieve/pii/S1359646224001866.

[26] S. Chakraborty, C.S. Patil, S.R. Niezgoda, Development of the cube component {001}<100> during plane strain compression of copper and its importance in recrystallization nucleation, Metall. Mater. Trans. A 53 (2) (2022) 503–522, http://dx.doi.org/10.1007/s11661-021-06513-0, ISSN 1073-5623, 1543-1940. URL https://link.springer.com/10.1007/s11661-021-06513-0.

[27] M. Diehl, L. Kertsch, K. Traka, D. Helm, D. Raabe, Site-specific quasi in situ investigation of primary static recrystallization in a low carbon steel, Mater. Sci. Eng. A 755 (2019) 295–306, http://dx.doi.org/10.1016/j.msea.2019.02.032, ISSN 09215093. URL https://linkinghub.elsevier.com/retrieve/pii/S0921509319301959.

[28] K. Traka, K. Sedighiani, C. Bos, J. Galan Lopez, K. Angenendt, D. Raabe, J. Sietsma, Topological aspects responsible for recrystallization evolution in an IF-steel sheet – investigation with cellular-automaton simulations, Comput. Mater. Sci. 198 (2021) 110643, http://dx.doi.org/10.1016/j.commatsci.2021.110643, ISSN 09270256. URL https://linkinghub.elsevier.com/retrieve/pii/S0927025621003700.

[29] K. Traka, Investigations of the early stages of recrystallization in interstitial-free and low-carbon steel sheets (Ph.D. thesis), Delft University of Technology, 2022, http://dx.doi.org/10.4233/UUID:962F6655-A1B8-4C38-8467-0B2B651AB629, URL http://resolver.tudelft.nl/uuid:962f6655-a1b8-4c38-8467-0b2b651ab629.

[30] K. Song, H. Ding, C. Zhang, L. Zhang, G. Deng, H. Zheng, High-resolution simulating of grain substructure in cold rolling and its effects on primary recrystallization in annealing of ferritic stainless steel, J. Mater. Res. Technol. 30 (2024) 40–51, http://dx.doi.org/10.1016/j.jmrt.2024.03.065, ISSN 22387854. URL https://linkinghub.elsevier.com/retrieve/pii/S2238785424005969.

[31] A. Kalaki, H. Vafaeenezhad, D. Mirahmadi, J. Hirsch, A computational approach to restoration phenomena during annealing of rolled Cu-2Be: recrystallization, grain growth and abnormal grain growth, Modelling Simul. Mater. Sci. Eng. 31 (6) (2023) 065018, http://dx.doi.org/10.1088/1361-651X/acea3a, ISSN 0965-0393, 1361-651X. URL https://iopscience.iop.org/article/10.1088/1361-651X/acea3a.

[32] M. Diehl, M. Kühbach, Coupled experimental-computational analysis of primary static recrystallization in low carbon steel, Modelling Simul. Mater. Sci. Eng. 28 (1) (2020) 014001, http://dx.doi.org/10.1088/1361-651X/ab51bd, ISSN 0965-0393, 1361-651X. URL https://iopscience.iop.org/article/10.1088/1361-651X/ab51bd.

[33] Y. Suwa, M. Tomita, Y. Tanaka, K. Ushioda, Phase-field simulation of recrystallization in cold rolling and subsequent annealing of pure iron exploiting EBSD data of cold-rolled sheet, ISIJ Int. 61 (1) (2021) 350–360, http://dx.doi.org/10.2355/isijinternational.ISIJINT-2020-226, ISSN 0915-1559, 1347-5460. URL https://www.jstage.jst.go.jp/article/isijinternational/61/1/61_ISIJINT-2020-226/_article.

[34] M. Kuwahara, K. Hachimura, S. Eiho, M. Kinoshita, Processing of RI-angiocardiographic images, in: K. Preston, M. Onoe (Eds.), Digital Processing of Biomedical Images, Springer US, Boston, MA, 1976, pp. 187–202, http://dx.doi.org/10.1007/978-1-4684-0769-3_13, ISBN 978-1-4684-0771-6 978-1-4684-0769-3. URL http://link.springer.com/10.1007/978-1-4684-0769-3_13.

[35] A. Winkelmann, B.M. Jablon, V.S. Tong, C. Trager-Cowan, K.P. Mingard, Improving EBSD precision by orientation refinement with full pattern matching, J. Microsc. 277 (2) (2020) 79–92, http://dx.doi.org/10.1111/jmi.12870, ISSN 0022-2720, 1365-2818. URL https://onlinelibrary.wiley.com/doi/10.1111/jmi.12870.

[36] J.G. Kemeny, Theory of self-reproducing automata. John von Neumann. edited by Arthur W. Burks. university of Illinois press, urbana, 1966. 408 pp., illus. $10, Science 157 (3785) (1967) 180, http://dx.doi.org/10.1126/science.157.3785.180, ISSN 0036-8075, 1095-9203. URL http://www.sciencemag.org/cgi/doi/10.1126/science.157.3785.180.

[37] D. Raabe, Computational Materials Science: The Simulation of Materials, Microstructures and Properties, first ed., Wiley, 1998, http://dx.doi.org/10.1002/3527601945, ISBN 978-3-527-29541-8 978-3-527-60194-3. URL https://onlinelibrary.wiley.com/doi/book/10.1002/3527601945.

[38] K. Traka, J. Sietsma, M.J. Santofimia Navarro, Modeling the interaction of carbon segregation to defects and carbon partitioning in multiphase steels, Acta Mater. 277 (2024) 120204, http://dx.doi.org/10.1016/j.actamat.2024.120204, ISSN 13596454. URL https://linkinghub.elsevier.com/retrieve/pii/S1359645424005548.

[39] C. Bos, M.G. Mecozzi, J. Sietsma, A microstructure model for recrystallisation and phase transformation during the dual-phase steel annealing cycle, Comput. Mater. Sci. 48 (3) (2010) 692–699, http://dx.doi.org/10.1016/j.commatsci.2010.03.010, ISSN 09270256. URL http://linkinghub.elsevier.com/retrieve/pii/S0927025610001242.

[40] C. Bos, M.G. Mecozzi, D.N. Hanlon, M.P. Aarnts, J. Sietsma, Application of a three-dimensional microstructure evolution model to identify key process settings for the production of dual-phase steels, Metall. Mater. Trans. A 42 (12) (2011) 3602–3610, http://dx.doi.org/10.1007/s11661-011-0696-x, ISSN 1073-5623, 1543-1940. URL http://link.springer.com/10.1007/s11661-011-0696-x.

[41] V. Shah, K. Sedighiani, J.S. Van Dokkum, C. Bos, F. Roters, M. Diehl, Coupling crystal plasticity and cellular automaton models to study meta-dynamic recrystallization during hot rolling at high strain rates, Mater. Sci. Eng. A 849 (2022) 143471, http://dx.doi.org/10.1016/j.msea.2022.143471, ISSN 09215093. URL https://linkinghub.elsevier.com/retrieve/pii/S0921509322008590.

[42] A. Després, M. Greenwood, C.W. Sinclair, A mean-field model of static recrystallization considering orientation spreads and their time-evolution, Acta Mater. 199 (2020) 116–128, http://dx.doi.org/10.1016/j.actamat.2020.08.013, ISSN 13596454. URL https://linkinghub.elsevier.com/retrieve/pii/S1359645420306108.

[43] A. Després, J.D. Mithieux, C.W. Sinclair, Modelling the relationship between deformed microstructures and static recrystallization textures: Application to ferritic stainless steels, Acta Mater. 219 (2021) 117226, http://dx.doi.org/10.1016/j.actamat.2021.117226, ISSN 13596454. URL https://linkinghub.elsevier.com/retrieve/pii/S1359645421006066.

[44] A.D. Rollett, D.J. Srolovitz, M.P. Anderson, Simulation and theory of abnormal grain growth—anisotropic grain boundary energies and mobilities, Acta Metall. 37 (4) (1989) 1227–1240, http://dx.doi.org/10.1016/0001-6160(89)90117-X, ISSN 00016160. URL https://linkinghub.elsevier.com/retrieve/pii/000161608990117X.

[45] F.J. Humphreys, A unified theory of recovery, recrystallization and grain growth, based on the stability and growth of cellular microstructures—I. the basic model, Acta Mater. 45 (10) (1997) 4231–4240.

[46] B. Hutchinson, Nucleation of recrystallisation, Scr. Metall. Mater. 27 (11) (1992) 1471–1475, http://dx.doi.org/10.1016/0956-716X(92)90130-7, ISSN 0956716X. URL https://linkinghub.elsevier.com/retrieve/pii/0956716X92901307.

[47] E.A. Holm, M.A. Miodownik, A.D. Rollett, On abnormal subgrain growth and the origin of recrystallization nuclei, Acta Mater. 51 (9) (2003) 2701–2716, http://dx.doi.org/10.1016/S1359-6454(03)00079-X, ISSN 13596454. URL https://linkinghub.elsevier.com/retrieve/pii/S135964540300079X.

[48] P. Bate, Modelling deformation microstructure with the crystal plasticity finite element method, Philos. Trans. R. Soc. Lond. Ser. A Math. Phys. Eng. Sci. 357 (1756) (1999) 1589–1601, http://dx.doi.org/10.1098/rsta.1999.0391, ISSN 1364-503X, 1471-2962. URL https://royalsocietypublishing.org/doi/10.1098/rsta.1999.0391.

[49] W.T. Read, W. Shockley, Dislocation models of crystal grain boundaries, Phys. Rev. 78 (3) (1950) 275–289, http://dx.doi.org/10.1103/PhysRev.78.275, ISSN 0031-899X. URL https://link.aps.org/doi/10.1103/PhysRev.78.275.

[50] D. Turnbull, Theory of grain boundary migration rates, JOM 3 (8) (1951) 661–665, http://dx.doi.org/10.1007/BF03397362, ISSN 1047-4838, 1543-1851. URL http://link.springer.com/10.1007/BF03397362.

[51] F.J. Humphreys, G.S. Rohrer, A.D. Rollett, Recrystallization And Related Annealing Phenomena, third ed., Elsevier, Amsterdam Oxford Cambridge, MA, 2017, ISBN 978-0-08-098269-4 978-0-08-098235-9.

[52] C. Hutchinson, H. Zurob, C. Sinclair, Y. Brechet, The comparative effectiveness of Nb solute and NbC precipitates at impeding grain-boundary motion in Nb steels, Scr. Mater. 59 (6) (2008) 635–637, http://dx.doi.org/10.1016/j.scriptamat.2008.05.036, ISSN 13596462. URL https://linkinghub.elsevier.com/retrieve/pii/S1359646208004272.

[53] M. Hillert, L. Hoglund, Mobility of α/γ phase interfaces in Fe alloys, Scr. Mater. 54 (7) (2006) 1259–1263, http://dx.doi.org/10.1016/j.scriptamat.2005.12.023, ISSN 13596462. URL https://linkinghub.elsevier.com/retrieve/pii/S1359646205008675.

[54] W.W. Mullins, Two-dimensional motion of idealized grain boundaries, J. Appl. Phys. 27 (8) (1956) 900–904, http://dx.doi.org/10.1063/1.1722511, ISSN 0021-8979, 1089-7550. URL http://aip.scitation.org/doi/10.1063/1.1722511.

[55] J. Von Neumann, Metal Interfaces, vol. 108, Cleveland.

[56] C.S. Smith, Grains, phases, and interphases: an interpretation of microstructure, Trans. Metall. Soc. AIME 175 (1948) 15–51, URL https://ui.adsabs.harvard.edu/abs/1948TrMS..175...15S.

[57] J.E. Burke, D. Turnbull, Recrystallization and grain growth, Prog. Met. Phys. 3 (1952) 220–292, http://dx.doi.org/10.1016/0502-8205(52)90009-9, ISSN 05028205. URL https://linkinghub.elsevier.com/retrieve/pii/0502820552900099.

[58] G. Gottstein, L.S. Shvindlerman, Grain Boundary Migration in Metals: Thermodynamics, Kinetics, Applications, second ed., CRC Series in Materials Science and Technology, Taylor & Francis, Boca Raton, 2010, ISBN 978-1-4200-5435-4.

[59] R.D. MacPherson, D.J. Srolovitz, The von Neumann relation generalized to coarsening of three-dimensional microstructures, Nature 446 (7139) (2007) 1053–1055, http://dx.doi.org/10.1038/nature05745, ISSN 0028-0836, 1476-4687. URL http://www.nature.com/articles/nature05745.

[60] L.S. Shvindlerman, G. Gottstein, A.D. Rollett, The Von Neumann-Mullins theory of grain growth – valid or not, Mater. Sci. Forum 467–470 (2004) 1111–1116, http://dx.doi.org/10.4028/www.scientific.net/MSF.467-470.1111, ISSN 1662-9752. URL https://www.scientific.net/MSF.467-470.1111.

[61] M. Hillert, On the theory of normal and abnormal grain growth, Acta Metall. 13 (3) (1965) 227–238, http://dx.doi.org/10.1016/0001-6160(65)90200-2, ISSN 00016160. URL https://linkinghub.elsevier.com/retrieve/pii/0001616065902002.

[62] M.P. Anderson, D.J. Srolovitz, G.S. Grest, P.S. Sahni, Computer simulation of grain growth—I. kinetics, Acta Metall. 32 (5) (1984) 783–791, http://dx.doi.org/10.1016/0001-6160(84)90151-2, ISSN 00016160. URL https://linkinghub.elsevier.com/retrieve/pii/0001616084901512.

[63] D. Raabe, F. Roters, F. Barlat, L.-Q. Chen (Eds.), Continuum Scale Simulation of Engineering Materials: Fundamentals - Microstructures - Process Applications, Wiley-VCH Verlag GmbH & Co. KGaA, Weinheim, FRG, 2004, http://dx.doi.org/10.1002/3527603786, ISBN 978-3-527-60378-7 978-3-527-30760-9. URL http://doi.wiley.com/10.1002/3527603786.

[64] K.G.F. Janssens, An introductory review of cellular automata modeling of moving grain boundaries in polycrystalline materials, Math. Comput. Simulation 80 (7) (2010) 1361–1381, http://dx.doi.org/10.1016/j.matcom.2009.02.011, ISSN 03784754. URL https://linkinghub.elsevier.com/retrieve/pii/S0378475409000470.

[65] A. Ayad, M. Ramoul, A.D. Rollett, F. Wagner, Quantifying primary recrystallization from EBSD maps of partially recrystallized states of an IF steel, Mater. Charact. 171 (2021) 110773, http://dx.doi.org/10.1016/j.matchar.2020.110773, ISSN 10445803. URL https://linkinghub.elsevier.com/retrieve/pii/S1044580320322440.

[66] K. Ushioda, W.B. Hutchinson, Role of shear bands in annealing texture formation in 3%Si-Fe(111)[112] single crystals, ISIJ Int. 29 (10) (1989) 862–867, http://dx.doi.org/10.2355/isijinternational.29.862, ISSN 0915-1559. URL http://joi.jlc.jst.go.jp/JST.Journalarchive/isijinternational1989/29.862?from=CrossRef.

[67] K. Verbeken, L. Kestens, M.D. Nave, Re-evaluation of the Ibe–Lücke growth selection experiment in a Fe–Si single crystal, Acta Mater. 53 (9) (2005) 2675–2682, http://dx.doi.org/10.1016/j.actamat.2005.02.030, ISSN 13596454. URL https://linkinghub.elsevier.com/retrieve/pii/S135964540500128X.

[68] Über die spontane Keimbildung bei der Herstellung von Einkristallen durch Rekristallisation. 2. issn 00234753, 15214079, doi: 10.1002/crat.19670020204. URL http://doi.wiley.com/10.1002/crat.19670020204.

[69] P. Gobernado, R.H. Petrov, L.A.I. Kestens, Recrystallized {311} < 136 > orientation in ferrite steels, Scr. Mater. 66 (9) (2012) 623–626, http://dx.doi.org/10.1016/j.scriptamat.2012.01.056, ISSN 13596462. URL http://linkinghub.elsevier.com/retrieve/pii/S1359646212000838.